



**Michigan
Technological
University**

Michigan Technological University
Digital Commons @ Michigan Tech

Michigan Tech Publications, Part 2

1-2-2024

Thermo-photo catalytic anode process for carbonate-superstructured solid fuel cells

Hanrui Su

Michigan Technological University, hanruis@mtu.edu

Yun Hang Hu

Michigan Technological University, yunhangh@mtu.edu

Follow this and additional works at: <https://digitalcommons.mtu.edu/michigantech-p2>

 Part of the [Materials Science and Engineering Commons](#)


Recommended Citation

Su, H., & Hu, Y. (2024). Thermo-photo catalytic anode process for carbonate-superstructured solid fuel cells. *Proceedings of the National Academy of Sciences of the United States of America*, 121(2).

<http://doi.org/10.1073/pnas.2314996121>

Retrieved from: <https://digitalcommons.mtu.edu/michigantech-p2/444>

Follow this and additional works at: <https://digitalcommons.mtu.edu/michigantech-p2>

 Part of the [Materials Science and Engineering Commons](#)



Thermo-photo catalytic anode process for carbonate-superstructured solid fuel cells

Hanrui Su^a and Yun Hang Hu^{a,1}

Edited by Zili Wu, Oak Ridge National Laboratory, Oak Ridge, TN; received August 29, 2023; accepted November 16, 2023 by Editorial Board Member Shaul Mukamel

Converting hydrocarbons and greenhouse gases (i.e., carbon dioxide, CO₂) directly into electricity through fuel cells at intermediate temperatures (450 to 550 °C) remains a significant challenge, primarily due to the sluggish activation of C–H and C=O bonds. Here, we demonstrated a unique strategy to address this issue, in which light illumination was introduced into the thermal catalytic CO₂ reforming of ethane in the anode as a unique thermo-photo anode process for carbonate-superstructured solid fuel cells. The light-enhanced fuel activation led to excellent cell performance with a record-high peak power density of 168 mW cm⁻² at an intermediate temperature of 550 °C. Furthermore, no degradation was observed during ~50 h operation. Such a successful integration of photo energy into the fuel cell system provides a new direction for the development of efficient fuel cells.

catalysis | fuel cell | ethane | thermo-photo

In recent years, the increase in anthropogenic carbon dioxide (CO₂) emissions and the presence of significant shale gas reserves have prompted extensive research on effective methods of utilizing these greenhouse gases. Carbon capture and utilization technologies, especially for CO₂ reduction, show great potential in mitigating environmental concerns and promoting a sustainable carbon cycle (1, 2). Efficient fuel cells are required to provide clean and sustainable energy solutions with minimal environmental impact and mitigating the effect of climate change (3). Among these, solid oxide fuel cells (SOFCs) have emerged as promising energy devices for generating electric power from hydrocarbons, shale gas, and renewable fuels (4, 5). However, their high operating temperatures (such as 800 °C) pose challenges in terms of system costs, complexity, and durability. To make SOFCs more economically competitive and commercially viable, substantial efforts have focused on reducing the operating temperature to minimize material degradation, lower the risk of leaks, and utilize less expensive components (6–8). However, the development of low-temperature SOFCs is hindered by polarization losses due to sluggish hydrocarbon oxidation and coke formation (9). Recently, we introduced a different approach to address this challenge by creating a highly efficient solid fuel cell called the “carbonate-superstructured solid fuel cell” (CSSFC) (10). A superstructured carbonate layer on the surface of a porous ceramic oxide electrolyte was in situ generated in CSSFC, achieving exceptional electrochemical performance and ultrahigh ionic conductivity at a relatively low operating temperature of around 500 °C. Unlike conventional SOFCs that rely on oxygen ion transfer through a dense solid electrolyte thin film or molten carbonate fuel cells that involve carbonate ion transfer with continuous CO₂ feeding, the CSSFC operates via rapid oxygen ion transfer at the interface between melted carbonates and solid doped ceria electrolyte, even at lower temperatures. While the CSSFC offers the potential for converting hydrocarbons into electricity, the direct electrochemical oxidation at low operating temperatures still presents performance limitations (10).

The thermally catalytic dry reforming of hydrocarbons into hydrogen (H₂) and carbon monoxide (CO) is essential due to the faster electro-oxidation of hydrogen than hydrocarbons (9). However, conventional dry reforming of methane (DRM) or ethane (C₂H₆) on state-of-the-art SOFC anode surfaces faces limitations in terms of thermodynamic conversion constraints and high thermal energy requirements (11, 12). Therefore, a significant challenge lies in lowering the reaction temperature for efficient dry reforming reaction. In recent developments, the inclusion of photo energy has emerged as a promising solution to overcome the challenges associated with dry reforming reactions. It enables efficient and lower-temperature reforming processes, enhances catalytic stability, and avoids detrimental effects such as self-poisoning and byproduct formation (13–17). For instance, the DRM over a Pt/black TiO₂ catalyst achieved highly efficient hydrogen production at a low-temperature of 550 °C under visible-light irradiation, in contrast to negligible

Significance

So far, the operation energy of solid oxide fuel cells is thermal energy, leading to insufficient activation of hydrocarbon fuels with cell polarization losses at low-temperatures. To solve the issue, we introduced photo energy into the anode to create a unique thermo-photo anode process for carbonate-superstructured solid fuel cell. This greatly boosted the fuel activation via the thermo-photo hybrid catalytic process, achieving a record-high peak power density at 550 °C. This finding presents a promising pathway for ultimately advancing the efficiency and performance of solid fuel cells.

Author affiliations: ^aDepartment of Materials Science and Engineering, Michigan Technological University, Houghton, MI 49931-1295

Author contributions: Y.H.H. designed research; H.S. performed research; H.S. and Y.H.H. analyzed data; and H.S. and Y.H.H. wrote the paper.

The authors declare no competing interest.

This article is a PNAS Direct Submission. Z.W. is a guest editor invited by the Editorial Board.

Copyright © 2024 the Author(s). Published by PNAS. This article is distributed under Creative Commons Attribution-NonCommercial-NoDerivatives License 4.0 (CC BY-NC-ND).

¹To whom correspondence may be addressed. Email: yunhangh@mtu.edu.

This article contains supporting information online at <https://www.pnas.org/lookup/suppl/doi:10.1073/pnas.2314996121/-/DCSupplemental>.

Published January 2, 2024.

hydrogen production in the dark (18). Similar improvements have been demonstrated for the partial oxidation of ethane using Au nanoparticles supported on WO_3 (19, 20). Moreover, it is anticipated that light irradiation enhances catalytic stability and plays a synergistic role in activating methane (CH_4) and CO_2 , facilitating the coupling of their dissociating species (21). This synergy minimizes the self-poisoning effect caused by different reactants (CH_4 and CO_2) and prevents the formation of undesired byproducts such as coke.

As a representative fuel gas, ethane is the second most abundant component (3 to 12%) in shale gas (22, 23). However, ethane has attracted little attention for solid fuel cells due to its low activity at low-temperature and high coke formation in the anode (5, 24). This situation inspired us to introduce light illumination into thermal catalytic dry reforming of ethane in the CSSFC anode, creating a unique thermo-photo anode process with Pt/black TiO_2 catalyst in this work and thus achieving a record-high peak power density (PPD) of 168 mW cm^{-2} and excellent cell stability at an intermediate temperature of $550 \text{ }^\circ\text{C}$.

To fabricate the anode for the thermo-photo catalytic activation of ethane fuel in CSSFCs, we employed a porous Ni-BaZr_{0.1}Ce_{0.7}Y_{0.1}Yb_{0.1}O_{3-δ} (BZCYYb) anode layer due to its high activity for hydrocarbon oxidation. Furthermore, this layer was co-pressed onto a Ce_{0.8}Sm_{0.2}O₂ (SDC) electrolyte and an LiNi_{0.8}Co_{0.15}Al_{0.05}O₂ (NCAL) cathode layer, facilitating the formation of an interfacial carbonate/solid oxide highway for efficient oxide ion conduction. Then, we introduced an upper anode catalyst layer (ACL) comprising a highly active thermo-photo Pt/black TiO_2 reforming catalyst. This catalyst played a crucial role in catalyzing the reforming of C_2H_6 with CO_2 under light irradiation, resulting in the production of H_2 and CO . These in situ-generated products will be

electrochemically oxidized to CO_2 ($\text{CO} + \text{O}^{2-} \rightarrow \text{CO}_2 + 2\text{e}^-$) and H_2O ($\text{H}_2 + \text{O}^{2-} \rightarrow \text{H}_2\text{O} + 2\text{e}^-$) on or near the anode–electrolyte interface by oxide ions (O^{2-}). The generated electrons flow through the external electrical circuit (Fig. 1A). As shown in Fig. 1B, one can see a representative scanning electron micrograph (SEM) cross-sectional view of a CSSFC, depicting a porous SDC electrolyte ($\sim 400 \mu\text{m}$) sandwiched between a porous Ni-BZCYYb anode ($\sim 600 \mu\text{m}$) and an NCAL cathode layer ($\sim 400 \mu\text{m}$). Furthermore, Fig. 1C and D provide typical cross-sectional and top-down views of the porous ACL ($\sim 100 \mu\text{m}$) on the anode, respectively.

The electrochemical performance of the CSSFCs was assessed by directly utilizing a C_2H_6 – CO_2 (1:1) mixture gas as the fuel and ambient air as the oxidant. The evaluations were conducted at $550 \text{ }^\circ\text{C}$ both in the dark and under simulated sunlight illumination using a thermo-photo experimental setup (SI Appendix, Fig. S1). As shown in Fig. 1E, the PPD reached 168 mW cm^{-2} at $550 \text{ }^\circ\text{C}$ under simulated sunlight illumination (1 sun). This PPD value is significantly higher compared to the recently reported values ($\sim 100 \text{ mW cm}^{-2}$) for a protonic ceramic fuel cell fueled with ethane at approximately $700 \text{ }^\circ\text{C}$ (25–27). Fig. 1F and SI Appendix, Fig. S2 show a moderate but consistent increase in PPDs when light irradiation is applied to the ACL across temperatures ranging from 475 to $550 \text{ }^\circ\text{C}$, resulting in an enhancement of up to approximately 17% compared to the fuel cell operated in the dark. These indicate the significant role of light irradiation in enhancing performance. Fig. 1G illustrates the voltages of the CSSFC operated at $550 \text{ }^\circ\text{C}$ under a constant current density of 100 mA cm^{-2} for approximately 50 h. Only a slight voltage drop at around the 20th hour occurred probably due to a fluctuation in light irradiation, which is supported by almost no structure change in anode (SI Appendix, Fig. S3) and photocatalyst (SI Appendix, Figs. S13 and S14) during 50 h operation. Afterward,

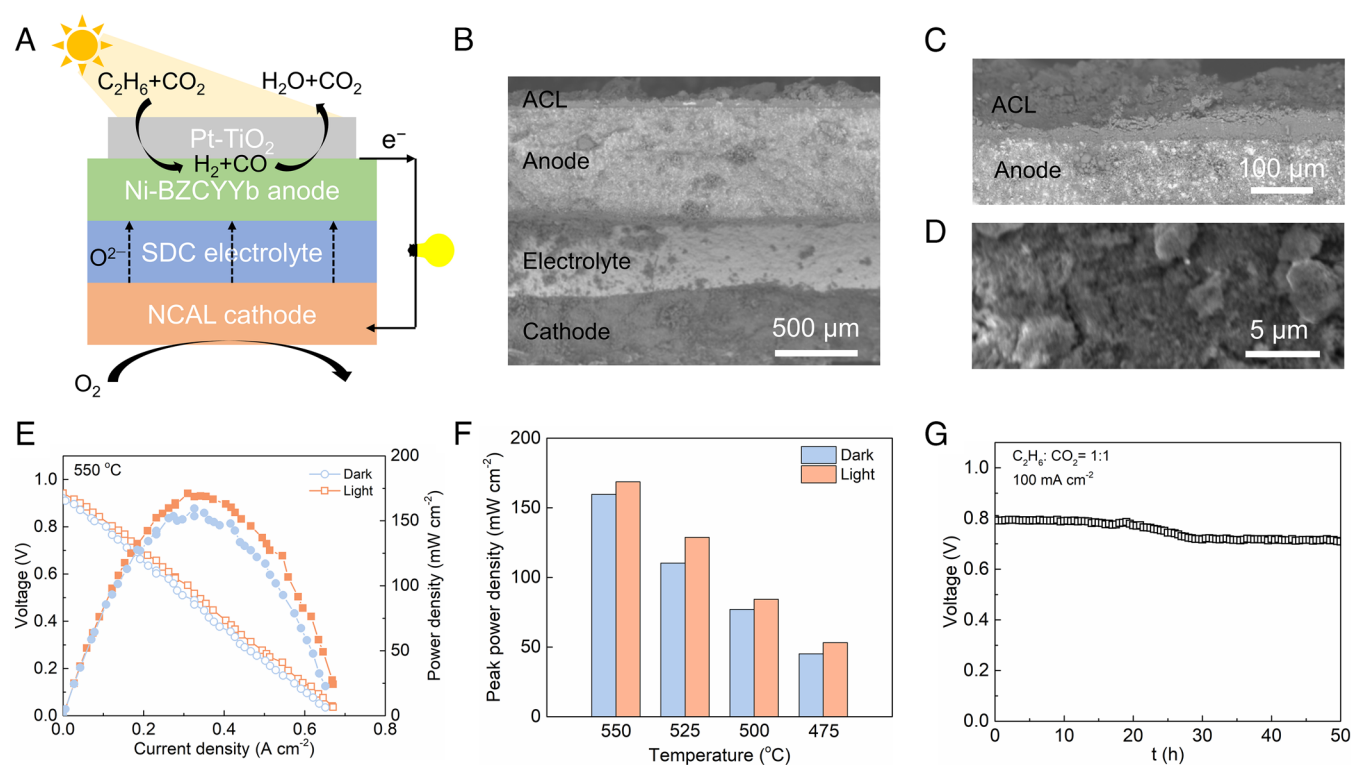


Fig. 1. Structure and performance of the CSSFCs. (A) Schematics of CSSFC with thermo-photo catalytic anode process. (B) A SEM of a CSSFC, including a cathode, an electrolyte, an anode, and an ACL. (C) A cross-sectional view of the anode and the ACL. (D) A top-down view of the ACL. (E) Polarization and power density curves of CSSFCs operated at $550 \text{ }^\circ\text{C}$ using C_2H_6 – CO_2 (1:1) as the fuel and ambient air as the oxidant. (F) Comparison of peak power densities at 475 to $550 \text{ }^\circ\text{C}$ with or without simulated sunlight irradiation. (G) Voltage curve under operation with C_2H_6 – CO_2 (1:1) at $550 \text{ }^\circ\text{C}$ and a constant current density of 0.1 A cm^{-2} .

the stable power output ($\sim 72 \text{ mW cm}^{-2}$ at 0.72 V) with $\text{C}_2\text{H}_6\text{-CO}_2$ (1:1) fuel was obtained, demonstrating the robustness of our photo-enhanced CSSFC in direct utilization of ethane and CO_2 and thus the excellent durability. Notably, the multifunctional anode exhibits exceptional coking resistance, as evidenced by the absence of coking and delamination during continuous operation (SI Appendix, Fig. S3). Furthermore, the electrolyte layer becomes denser after cell operation, effectively preventing gas leakage (SI Appendix, Fig. S4). This densification can be attributed to the in situ-generated superstructured carbonates that plug microchannels between electrolyte nanoparticles (10).

To assess the catalytic efficiencies and light responses of various ACLs in the CSSFC, we conducted measurements over time while repeatedly switching the light on and off under a constant current load of 300 mA cm^{-2} . SI Appendix, Fig. S5 clearly demonstrates the excellent repeatability of the illumination effect. Among all tested catalysts, the ACL containing 1 wt.% Pt/black TiO_2 outperformed the others, indicating the superiority of the Pt/black TiO_2 catalyst for thermal-photo dry reforming of ethane. In this catalyst, Pt played a dual role by facilitating charge separation and exhibiting excellent activity in breaking C–H bonds (18). Although increasing the Pt loading from 0.5 to 1.0 wt.% promoted the light response, excessive Pt loading of 2.0 wt.% decreased performance (SI Appendix, Fig. S5). This could be attributed to Pt nanoparticles acting as recombination centers for electrons and holes, thereby negatively impacting the overall performance (28).

Electrochemical impedance spectroscopy (EIS) analysis was exploited to examine cell resistance under different conditions for deeper understanding of the impact of light on ion conduction and electrode reactions. The measurements were performed using $\text{C}_2\text{H}_6\text{-CO}_2$ (1:1) as the fuel at the anode and dry air at the cathode at $550 \text{ }^\circ\text{C}$ (Fig. 2A). By employing distribution of relaxation time (DRT) analysis, we deconvoluted the contributions of each process in the dark and under light illumination. The DRT profiles were divided into three regions: the high-frequency region (P_{HF}) characterizing ionic bulk diffusion and transfer processes, the intermediate

frequency region (P_{IF}) associated with surface exchange processes and charge transfer, and the low-frequency region (P_{LF}) representing mass transfer processes such as gas diffusion within the anode pores (29). Under light irradiation, the integral area of P_{HF} remained almost unchanged, whereas the integral areas of P_{LF} and P_{IF} significantly decreased (Fig. 2B). This suggests that photo energy enhances the surface exchange capability of $\text{C}_2\text{H}_6/\text{CO}_2$ and improves fuel gas diffusion, leading to reduced polarization resistance and enhanced electrochemical performance. Furthermore, area-specific resistance components derived from Nyquist plots were also analyzed (SI Appendix, Fig. S6). We observed a substantial reduction in the temperature-dependent ohmic resistance (R_o) values of the CSSFCs under light irradiation within a temperature range of 475 to $525 \text{ }^\circ\text{C}$ (Fig. 2C). Specifically, the CSSFCs with light exhibited a higher total ionic conductivity of 0.06 S cm^{-1} at $500 \text{ }^\circ\text{C}$, compared to 0.05 S cm^{-1} without light irradiation. The activation energy of the total ionic conductivity with light (0.66 eV) was also lower than that without light (0.78 eV) due to the opto-ionic effect, namely, the accumulation of photo-generated charge carriers at the grain boundary core of metal oxide could decrease the grain boundary space charge potential, leading to lower resistance and activation energy for ion transfer at grain boundaries or interfaces (30). Moreover, the temperature-dependent polarization resistance (R_p) values of the CSSFC under $\text{C}_2\text{H}_6\text{-CO}_2/\text{air}$ conditions with light irradiation decreased significantly from 3.25, 1.79, 1.15, and $0.76 \text{ } \Omega \text{ cm}^2$ at four temperatures in the range from 475 to $550 \text{ }^\circ\text{C}$, respectively (Fig. 2D). This further confirms the substantial role played by light illumination in reducing cell polarization resistance and compensating for losses at lower temperatures.

The functionality of ACLs in the CSSFCs was evaluated by analyzing the effluent stream composition from the fuel cell being operated at open circuit voltage (OCV) within a temperature range of 475 to $550 \text{ }^\circ\text{C}$ (SI Appendix, Fig. S7). Under OCV conditions, a typical gas composition of approximately 6% CO , 2% H_2 , and the remaining C_2H_6 ($\sim 46\%$) and CO_2 ($\sim 46\%$) suggests that the

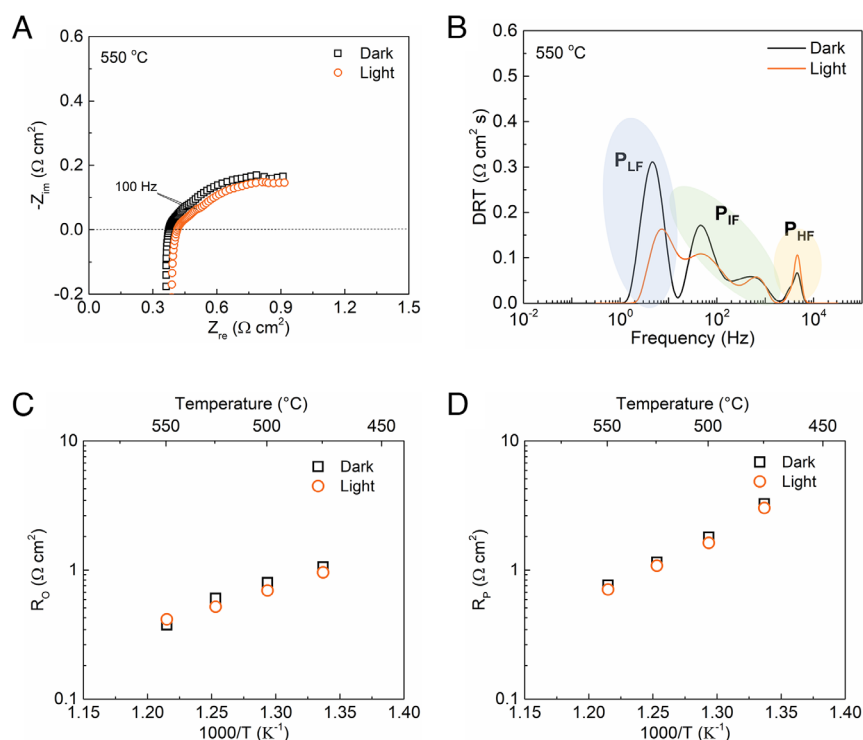


Fig. 2. EIS measurements for the CSSFCs with or without simulated sunlight irradiation. (A) Impedance spectra of CSSFCs operated with $\text{C}_2\text{H}_6\text{-CO}_2$ (1:1) at $550 \text{ }^\circ\text{C}$. (B) DRT analysis of the CSSFCs operated with $\text{C}_2\text{H}_6\text{-CO}_2$ (1:1) at $550 \text{ }^\circ\text{C}$. Temperature dependence of (C) ohmic resistance (R_o) and (D) polarization resistance (R_p) of CSSFCs using $\text{C}_2\text{H}_6\text{-CO}_2$ (1:1) as fuel and ambient air as oxidant.

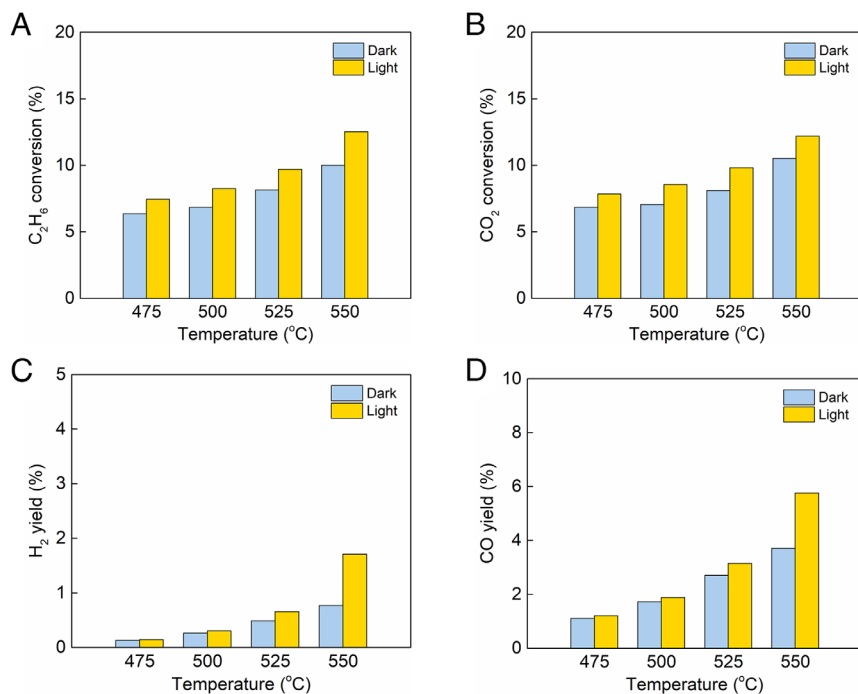


Fig. 3. The catalytic performance of the anode with or without simulated sunlight irradiation. (A) C₂H₆ conversion, (B) CO₂ conversion, (C) H₂ yield, and (D) CO yield of the CSSFCs with C₂H₆-CO₂ (1:1) (~100 mL min⁻¹) fed to the anode at 475 to 550 °C.

dominant catalytic reaction is dry reforming involving C–C bond cleavage ($\text{C}_2\text{H}_6 + 2\text{CO}_2 \rightarrow 4\text{CO} + 3\text{H}_2$, $\Delta H = 428$ kJ/mol). This pathway takes advantage of the thermodynamically favorable cleavage of the C–C bond ($\text{CH}_3\text{--CH}_3$, 368 kJ/mol) over the C–H bond of ethane ($\text{C}_2\text{H}_5\text{--H}$, 415 kJ/mol) (22). To gain further insights into the detailed mechanism of electrode reactions under light, we investigated the reactant conversions and product yields for dry reforming of ethane. As shown in Fig. 3, one can see temperature dependences of the conversion of C₂H₆ and CO₂ as well as the yield of H₂ and CO. Namely, the conversion of C₂H₆/CO₂ and the yield of H₂/CO increase with rising operation temperature. Under light irradiation, the conversion of C₂H₆ and CO₂ on the anode at 550 °C reaches approximately 12.5 and 12.2%, respectively, which is about 25% higher than the conversion without light (10.0% for C₂H₆ and 10.5% for CO₂). The apparent activation energies for C₂H₆ and CO₂ conversion over the anode with light were determined to be 35.0 and 29.7 kJ mol⁻¹, respectively (SI Appendix, Fig. S8). These indicate that the light illumination enhanced catalytic activity for C₂H₆ and CO₂ conversion and the impact of illumination becomes more pronounced at higher temperatures. At 550 °C, the yields of H₂ and CO under light irradiation are approximately 1.7 and 5.7%, respectively, which are about 100 and 50% higher than the yields under dark conditions (0.8% for H₂ and 3.7% for CO). The H₂/CO ratio increases from 0.12 to 0.30 with increasing temperature. This happened probably because the dry reforming reaction is more endothermic than the reverse water-gas shift reaction (RWGS, $\text{H}_2 + \text{CO}_2 \rightarrow \text{CO} + \text{H}_2\text{O}$) (23).

The cell performance is also influenced by C₂H₆/CO₂ ratio. Pure C₂H₆ did not exhibit a significant response to light illumination, whereas a substantial light response was observed for the C₂H₆/CO₂ mixture gas (SI Appendix, Fig. S9). The C₂H₆ conversion increased from 7.9 to 12.5% and then decreased to 1.6% with increasing CO₂ concentration at 550 °C under light illumination (SI Appendix, Figs. S10 and S11). Furthermore, the conversion of CO₂ exceeded that of C₂H₆ at all temperatures, indicating the contribution of simultaneous RWGS (23). Thus, using a C₂H₆/CO₂ feed molar ratio of 1:1 instead of 2:1 or 1:2

clearly leads to better catalytic performance and improved utilization of both reactants, which is consistent with the highest power density obtained at the C₂H₆/CO₂ ratio of 1:1 (SI Appendix, Fig. S9). Furthermore, the yields of H₂ and CO were significantly enhanced under light illumination for various compositions of C₂H₆/CO₂ mixture gas, further confirming the promoting role of thermo-photo catalysis.

The universal influence of thermo-photo catalysis on fuel cell performance enhancement was demonstrated by evaluating the polarization curves of CSSFCs using C₂H₆ (3% H₂O) as the fuel. SI Appendix, Fig. S12 shows peak power densities of 152, 113, 81, and 45 mW cm⁻² under light illumination at 550, 525, 500, and 475 °C, respectively, which were significantly higher than those (139, 108, 63, and 42 mW cm⁻²) under dark conditions. The cell exhibited a much lower R_p value (0.86 Ω cm²) at 550 °C under light illumination than that (1.15 Ω cm²) in dark condition. These findings highlight the superiority of light illumination in both dry and steam reforming of ethane, emphasizing the universal role of thermo-photo catalysis in enhancing fuel cell performance.

The microstructure of the Pt/black TiO₂ catalyst was evaluated using scanning transmission electron microscopy (STEM). As shown in Fig. 4, distinct Pt nanoparticles were uniformly dispersed on the external surface of TiO₂. In the High-resolution transmission electron microscopy (HRTEM) image (Fig. 4A), one can see lattice fringes with d-spacings of 0.24 and 0.23 nm, corresponding to the (103) plane of anatase TiO₂ and the (111) plane of metallic Pt, respectively. Furthermore, the high-angle annular dark-field (HAADF) images combined with energy-dispersive X-ray spectra (EDS) in STEM mode (Fig. 4B and C) revealed the homogeneous distribution of Pt, Ti, and O elements. The average size of Pt nanoparticles was found to be as small as 1.44 nm (Fig. 4D), indicating a high proportion of Pt atoms located near the Pt–TiO₂ interface. After a 50 h test, the bright-field TEM image showed that the average particle size remained the same as the initial size, and no evidence of coke formation was observed on the catalyst, indicating excellent stability of the TiO₂ crystal structure (SI Appendix, Fig. S13). Additionally, the size of Pt nanoparticles slightly increased to approximately 1.70 nm (SI Appendix, Fig. S14), further confirming the stability of the Pt

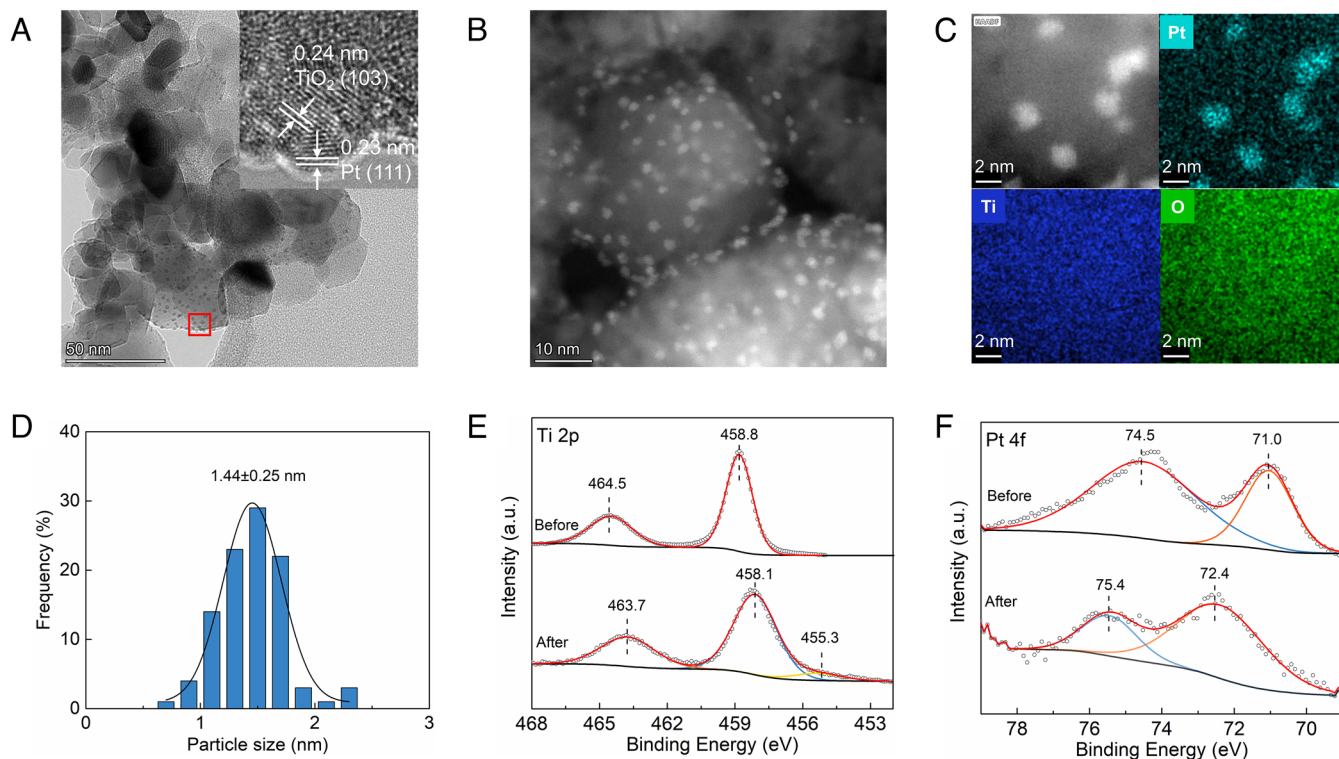


Fig. 4. Characterization of Pt/black TiO_2 catalyst. (A) TEM image and the *Inset* HRTEM image of the red square, (B) STEM image, (C) HAADF-STEM image and corresponding EDS elemental maps, and (D) Pt particle size distribution before the cell test. (E) Ti 2p XPS spectrum and (F) Pt 4f XPS spectrum before and after cell test.

nanoparticles. Furthermore, the surface properties of the catalyst were also evaluated by X-ray photoelectron spectrometer (XPS) measurements. Fig. 4E shows the Ti 2p XPS spectra of the initial catalyst, which are identical to the standard TiO_2 spectra (15). However, for the tested catalyst, the Ti 2p binding energies shifted downward, indicating an occurrence of upward surface band bending (28). Furthermore, the Ti $2p_{3/2}$ binding energy at 455.3 eV indicates the presence of Ti^{3+} species, suggesting a strong metal-support interaction between Pt and TiO_2 (31). The O 1s XPS spectra show a small peak at 531.5 eV (*SI Appendix, Fig. S15B*), confirming the existence of Ti-OH species on the catalyst's surface. In addition, the binding energies of Pt $4f_{7/2}$ and $4f_{5/2}$ shifted from 71.0 and 74.5 eV to 72.4 and 75.4 eV, respectively (Fig. 4F). These shifts could be attributed to the strong interactions between Pt atoms and surface O atoms of TiO_2 , promoting charge transfer from Pt to O (28).

In principle, a photocatalytic process has three basic requirements: a) the conduction band (CB) edge of the photocatalyst must be more negative than the redox potential of a reduction reaction, b) the valence band (VB) edge of the catalyst is more positive than the redox potential of an oxidation reaction, and c) the energy gap between the VB and the CB of the catalyst must ensure the excellent absorption of light (13). As shown by Ultraviolet (UV)-visible and Fourier transform near-infrared spectra (*SI Appendix, Fig. S16*), Pt/black TiO_2 absorbed not only UV light but also visible and near-infrared light, which is much better than Pt/ TiO_2 that can absorb mainly UV. This can be attributed to the generation of Ti^{3+} level below CB by 1.3 eV in black TiO_2 , leading to a small energy gap between Ti^{3+} and CB for visible and near-infrared light absorption (13). Furthermore, as shown by the energy band structure (*SI Appendix, Fig. S16E*), the CB edge is more negative than CO_2/CO redox potential, while the VB edge is more positive than the redox potential of $\text{CO}/\text{C}_2\text{H}_6$. This ensures the photocatalytic reaction of C_2H_6 and CO_2 to H_2 and CO.

Therefore, although the thermal catalytic reaction of C_2H_6 and CO_2 to H_2 and CO could take place in the CSSFC anode, the introduction of light into the anode created the photocatalytic reaction, leading to the thermo-photo hybrid catalytic process and thus enhancing the cell performance. On the other hand, as the operation temperature increases, the redox potential of CO_2/CO becomes more positive, while the redox potential of $\text{CO}/\text{C}_2\text{H}_6$ changes to more negative. This indicates that the introduction of thermal energy also enhanced the photocatalytic process. Notably, as demonstrated by a control experiment under dark conditions (*SI Appendix, Fig. S17*), the sunlight illumination caused only a small temperature increase ($\sim 5^\circ\text{C}$) on the anode surface and thus a negligible (less than 4%) increase in PPD, excluding the light-induced heating effect on the CSSFC performance.

In summary, a thermo-photo anode process was demonstrated as a unique chemical process for CSSFC with C_2H_6 and CO_2 as fuel. Compared with the regular thermal catalytic anode process, the thermo-photo hybrid catalytic anode process exhibited approximately 25% enhancement in the activation of C_2H_6 and CO_2 . As a result, a record-high PPD of 168 mW cm^{-2} was achieved at an intermediate temperature of 550°C . Furthermore, the cell exhibited excellent stability without degradation for ~ 50 h operation.

Materials and Methods

Material Synthesis. The reforming catalysts were synthesized using the impregnation method (15, 18). To prepare the 1 wt.% Pt/ TiO_2 catalyst, TiO_2 (P25, Sigma Aldrich) was impregnated with an aqueous solution of $\text{H}_2\text{PtCl}_6 \cdot 6\text{H}_2\text{O}$. The mixture was stirred until dry overnight at 25°C and then calcined at 550°C for 1 h. Subsequently, the obtained solid was subjected to a 50 mL/min H_2 gas flow at 550°C for 3 h, forming Pt/black TiO_2 catalyst. The preparation of the 1 wt.% Ru/ TiO_2 and Rh/ TiO_2 catalysts followed the same procedure as the Pt/ TiO_2 , but with $\text{RuCl}_3 \cdot \text{H}_2\text{O}$, $\text{RhCl}_3 \cdot 3\text{H}_2\text{O}$ as the respective precursors.

Cell Fabrication. The CSSFC was manufactured using the dry pressing method (10). Commercial $\text{LiNi}_{0.8}\text{Co}_{0.15}\text{Al}_{0.05}\text{O}_2$ (NCAL, NEI Corporation) powders were mixed with terpineol binder to create a slurry. This slurry was brush-painted onto Ni-foam and dried at approximately 60 °C for 12 h to serve as the cathode. The $\text{NiO-BaZr}_{0.1}\text{Ce}_{0.7}\text{Y}_{0.1}\text{Yb}_{0.1}\text{O}_{3-6}$ (BZCYYb) anode was prepared through a solid-state reaction. The $\text{Ce}_{0.8}\text{Sm}_{0.2}\text{O}_{1.9}$ (SDC) powders were synthesized using the carbonate co-precipitation process (10). The cell configuration of Ni-BZCYYb | SDC | NCAL was formed by uniaxial pressing, applying appropriate pressure to create a pellet. The pellet consisted of 0.35 g of NiO-BZCYYb anode powder, 0.25 g of SDC electrolyte powder, and NCAL-coated Ni-foam. The single porous cell had a thickness of approximately 2 mm and an active area of 0.64 cm². The ACL was fabricated through coating processes, where a mixture of reforming catalyst (20 mg Pt/TiO₂) and terpineol was printed onto the anode side of the pellets followed by calcinating at 550 °C for 1 h. It would be noted that the Pt/TiO₂ catalyst was in situ reduced into Pt/black TiO₂ by H₂ in the cell before operation.

Characterization. The crystal structures of the materials were analyzed using X-ray diffraction (XRD) with a Scintag XDS-2000 instrument, employing Cu K α radiation ($\lambda = 1.5406 \text{ \AA}$). XRD patterns were collected in the 2 θ range of 20° and 80° at a scanning rate of 2° per minute. The chemical states of the elements in the samples were examined using a PHI 5800 XPS equipped with a dual-source anode (Al and Mg). The reported binding energies were calibrated to adventitious carbon at a binding energy of 284.8 eV. The morphology of the catalysts was characterized using a FEI 200 kV Titan Themis STEM. The cross-section morphology of single cells was investigated using an environmental scanning electron microscope (Philips XL 40 instrument). The light absorption properties were determined by a Shimadzu UV-vis spectrophotometer (UV-2600) and a Bomem MB-160 near-infrared spectrometer. The gas compositions at the outlet were

analyzed using online gas chromatography (Hewlett-Packard 5890) coupled with a thermal conductivity detector.

Electrochemical Performance Measurements. The NiO-BZCYYb anode was reduced to Ni-BZCYYb by H₂ gas (99.999%) for 1 h at 550 °C before switching to the fuel gas. The anode side of the cell was supplied with a mixture of C₂H₆ and CO₂ (flow rate: ~100 mL/min) as the fuel, while the cathode side was supplied with ambient air (flow rate: ~300 mL/min) as the oxidant. The cell was placed inside a homemade reactor located in an electric furnace (refer to *SI Appendix, Fig. S1*). The anode surface was illuminated using a Xe lamp (Newport solar simulator) equipped with an AM 1.5 G filter, and the light intensity was maintained at 100 mW/cm². The I-V-P characteristics of the fuel cell were measured using an electronic load (IT8511, ITECH Electrical Co., Ltd.) with a scan rate of 0.02 A s⁻¹ in the current-voltage sweep. Additionally, EIS were obtained under OCV conditions using a CHI-760 electrochemical workstation (CH Instruments, Inc.) in the frequency range of 1 to 10⁵ Hz, with a voltage amplitude of 10 mV. The impedance spectra were analyzed using the ZSimpWin 3.60 software (EChem Software) to determine the electrolyte process and electrode process. The DRT calculation was performed using DRTtools (32). Mott-Schottky analyses were conducted in a three-electrode cell in which a fluorine-doped tin oxide glass coated with sample, Pt, and a saturated calomel electrode served as the working, counter, and reference electrodes, respectively (33). The electrolyte was 0.5 M sodium sulfate aqueous solution.

Data, Materials, and Software Availability. All study data are included in the article and/or *SI Appendix*.

ACKNOWLEDGMENTS. This work was partially supported by NSF (Grant Number CMMI-1661699).

- J. W. Zhang, C. D. Sewell, H. W. Huang, Z. Q. Lin, Closing the anthropogenic chemical carbon cycle toward a sustainable future via CO₂ valorization. *Adv. Energy Mater.* **11**, 2102767 (2021).
- W. Lai, Y. Qiao, J. Zhang, Z. Lin, H. Huang, Design strategies for markedly enhancing energy efficiency in the electrocatalytic CO₂ reduction reaction. *Energy Environ. Sci.* **15**, 3603–3629 (2022).
- M. Zhang, X. Xuan, W. Wang, C. Ma, Z. Lin, Anode photovoltage compensation-enabled synergistic CO₂ photoelectrocatalytic reduction on a flower-like graphene-decorated Cu foam cathode. *Adv. Funct. Mater.* **30**, 2005983 (2020).
- T. M. Gür, Comprehensive review of methane conversion in solid oxide fuel cells: Prospects for efficient electricity generation from natural gas. *Prog. Energy Combust. Sci.* **54**, 1–64 (2016).
- P. Boldrin *et al.*, Strategies for carbon and sulfur tolerant solid oxide fuel cell materials, incorporating lessons from heterogeneous catalysis. *Chem. Rev.* **116**, 13633–13684 (2016).
- E. D. Wachsman, K. T. Lee, Lowering the temperature of solid oxide fuel cells. *Science* **334**, 935–939 (2011).
- W. Zhang, Y. H. Hu, Progress in proton-conducting oxides as electrolytes for low-temperature solid oxide fuel cells: From materials to devices. *Energy Sci. Eng.* **9**, 984–1011 (2021).
- H. Su, Y. H. Hu, Progress in low-temperature solid oxide fuel cells with hydrocarbon fuels. *Chem. Eng. J.* **402**, 126235 (2020).
- Y. Chen *et al.*, A robust fuel cell operated on nearly dry methane at 500 °C enabled by synergistic thermal catalysis and electrocatalysis. *Nat. Energy* **3**, 1042–1050 (2018).
- H. Su, W. Zhang, Y. H. Hu, Carbonate-superstructured solid fuel cells with hydrocarbon fuels. *Proc. Natl. Acad. Sci. U.S.A.* **119**, e2208750119 (2022).
- Y. H. Hu, E. Ruckenstein, Comment on "Dry reforming of methane by stable Ni-Mo nanocatalysts on single-crystalline MgO". *Science* **368**, eabb5459 (2020).
- M. Li, Z. Sun, Y. H. Hu, Catalysts for CO₂ reforming of CH₄: A review. *J. Mater. Chem. A* **9**, 12495–12520 (2021).
- B. Han, Y. H. Hu, Highly efficient temperature-induced visible light photocatalytic hydrogen production from water. *J. Phys. Chem. C* **119**, 18927–18934 (2015).
- B. Han, W. Wei, M. Li, K. Sun, Y. H. Hu, A thermo-photo hybrid process for steam reforming of methane: Highly efficient visible light photocatalysis. *Chem. Commun. (Camb)* **55**, 7816–7819 (2019).
- S. Fang *et al.*, Photocatalytic hydrogen production over Rh-loaded TiO₂: What is the origin of hydrogen and how to achieve hydrogen production from water? *Appl. Catal., B* **278**, 119316 (2020).
- S. Fang, Y. H. Hu, Thermo-photo catalysis: A whole greater than the sum of its parts. *Chem. Soc. Rev.* **51**, 3609–3647 (2022).
- M. Li, Z. Sun, Y. H. Hu, Thermo-photo coupled catalytic CO₂ reforming of methane: A review. *Chem. Eng. J.* **428**, 131222 (2022).
- B. Han, W. Wei, L. Chang, P. Cheng, Y. H. Hu, Efficient visible light photocatalytic CO₂ reforming of CH₄. *ACS Catalysis* **6**, 494–497 (2016).
- Y. Zhu *et al.*, Highly efficient visible-light photocatalytic ethane oxidation into ethyl hydroperoxide as a radical reservoir. *Chem. Sci.* **12**, 5825–5833 (2021).
- Y. Zhu *et al.*, Distinct pathways in visible-light driven thermo-photo catalytic methane conversion. *J. Phys. Chem. Lett.* **12**, 7459–7465 (2021).
- F. Pan *et al.*, Integrating photocatalysis and thermocatalysis to enable efficient CO₂ reforming of methane on Pt supported CeO₂ with Zn doping and atomic layer deposited MgO overcoating. *Appl. Catal. B* **260**, 118189 (2020).
- Z. H. Xie *et al.*, Interfacial active sites for CO₂ assisted selective cleavage of C-C/C-H bonds in ethane. *Chem* **6**, 2703–2716 (2020).
- M. D. Porosoff *et al.*, Identifying different types of catalysts for CO₂ reduction by ethane through dry reforming and oxidative dehydrogenation. *Angew. Chem. Int. Ed. Engl.* **54**, 15501–15505 (2015).
- S. Park, J. M. Vohs, R. J. Gorte, Direct oxidation of hydrocarbons in a solid-oxide fuel cell. *Nature* **404**, 265–267 (2002).
- Y. Fan *et al.*, Barium-doped Sr₂Fe_{1.3}Mo_{0.3}O_{6.8} perovskite anode materials for protonic ceramic fuel cells for ethane conversion. *J. Am. Ceram. Soc.* **105**, 3613–3624 (2022).
- S. Lei *et al.*, Simultaneous generation of electricity, ethylene and decomposition of nitrous oxide via protonic ceramic fuel cell membrane reactor. *J. Energy Chem.* **77**, 359–368 (2023).
- M. Wang *et al.*, Nanostructured carbon as highly efficient and stable anodes for ethylene production and power generation in protonic ceramic electrochemical cells. *Carbon* **199**, 379–386 (2022).
- J. Zhang *et al.*, Regulation of energetic hot carriers on Pt/TiO₂ with thermal energy for photothermal catalysis. *Appl. Catal. B* **309**, 121263 (2022).
- S. Zhai *et al.*, A combined ionic Lewis acid descriptor and machine-learning approach to prediction of efficient oxygen reduction electrodes for ceramic fuel cells. *Nat. Energy* **7**, 866–875 (2022).
- T. Defferriere, D. Klotz, J. C. Gonzalez-Rosillo, J. L. M. Rupp, H. L. Tuller, Photo-enhanced ionic conductivity across grain boundaries in polycrystalline ceramics. *Nat. Mater.* **21**, 438–444 (2022).
- Z. Wu, Y. Li, W. Huang, Size-dependent Pt-TiO₂ strong metal-support interaction. *J. Phys. Chem. Lett.* **11**, 4603–4607 (2020).
- T. H. Wan, M. Saccoccio, C. Chen, F. Ciucci, Influence of the discretization methods on the distribution of relaxation times deconvolution: Implementing radial basis functions with DRTtools. *Electrochim. Acta* **184**, 483–499 (2015).
- S. Fang *et al.*, Turning dead leaves into an active multifunctional material as evaporator, photocatalyst, and bioplastic. *Nat. Commun.* **14**, 1203 (2023).